

Indentation of Deformable Plastic Layers

Thomasina Ball

December 10, 2017

1 Introduction

The indentation of deformable plastic layers has been studied extensively for determining the vertical bearing capacity of rigid strip footings. The solutions to this classic problem [14, 9] use the method of characteristics to determine an upper bound on the pressure underneath a vertically loaded indenter placed onto an idealised semi-infinite rigid-plastic foundation. These studies for a homogeneous half-space have been extended to consider non-homogeneous plastic solids [17, 15]; irregular shaped bodies [18]; rolling contacts [11, 4] and axisymmetric geometries [16, 6, 3]. The connection to a finite layer has also been considered for the plastic flow between two rough parallel plates being forced together [14, 9], with application to the flow near the end of a glacier [13]. However, apart from a few exceptions, most problems require numerical integration along characteristic curves to calculate the pressure.

More recently, the behaviour of a finite plastic layer has been explored through the use of viscoplastic fluids. Viscoplastic lubrication theory has been used to model the final shape of a two-dimensional slump [5] and the confined flow of viscoplastic fluid between rigid moving boundaries [8], where asymptotic expansion is based on the small aspect ratio ϵ . This formulation provides a more simple approach to calculating the plastic deformation of a shallow layer.

One application of studying the indentation of deformable plastic layers is in understanding the formation of footprints. Tracks and traces are of particular interest when studying extinct animals as they provide evidence for behaviour, paleoecology and evolution [7]. A number of studies have investigated the relationship between the indenter shape, the indentation left behind and the rheology of the substrate to try and deduce what characteristics can be determined from tracks and traces of distinct animals. Simple indentation models [1] have been used when looking at subfossil mammalian tracks in the Severn estuary. These experiments consisted of indenting an axisymmetric indenter into a layered plasticine structure and showed qualitative agreement with the essential features of track formation. Other experimental work has focused on practical field studies such [12] looking at live emus or clay. They found that footprints from the same trackmaker can appear morphologically different according to the properties of the sediment, and hence shows that care needs to be taken to understand the original rheological conditions of the substrate at the time of track making. More recently, numerical studies have been used to simulate the indentation of a deformable layer [2]. They used a finite-element simulation to study the depth versus

pressure exerted due to a rigid human foot indenting an elastic-plastic substrate with and without a firm subsurface layer. They found that depending on the depth of the initial deformable layer, regions either indented deeper or shallower than expected from the peak pressure in that region. This work demonstrated the importance of underfoot consolidation in altering when sediment is able to resist deformation under load and support larger pressures. These laboratory and numerical studies described above demonstrate the complexity of understanding the formation of footprints and the leading order effects substrate rheology and foot morphology can have. However, a simple quantitative approach to understanding the characteristics of footprints has yet to be taken.

In this study, we will explore the indentation of deformable plastic layers by building on the current advances in viscoplastic lubrication theory. In particular, we will consider the vertical indentation of a shallow viscoplastic layer by a flat-based and cylindrical indenter. We hope this will give insight the dominant balances in plastic deformation with application to footprint formation amongst many other interesting problems.

2 Theoretical Model: Loading

We wish to understand the deformation of a plastic layer by a rigid indenter. To do so we consider two stages: i) loading stage, where indentation is due to a given force, and ii) lift off stage, where the indenter lifts off the deformed substrate at a given speed. In all of the analysis to follow, we assume a two-dimensional geometry and that the motion of the indenter is always perpendicular to the substrate.

To model the substrate, we consider two different rheologies: a purely cohesive model with cohesion τ_Y to describe a mud-like substrate, and secondly a non-cohesive model with angle of friction ϕ to describe a granular substrate such as dry sand. During the loading stage, a rigid indenter deforms the substrate due to a given force F . We consider firstly the indentation of a shallow viscoplastic layer and then outline current theory for the indentation of a deep plastic layer.

2.1 Shallow layer

We use viscoplastic lubrication theory with a Bingham rheology as a vehicle for understanding a shallow plastic layer [8]. We consider the deformation of a uniform layer of viscoplastic fluid of height h_0 , density ρ , viscosity μ with an indenter of geometry $\eta(x)$, and characteristic length scale x_0 . The height of the indenter is given by $h(x, t) = \delta(t) + \eta(x)$, where $\delta(0) = h_0$, for $-L < x < L$ where L is the contact point on the indenter. The free-surface height of the fluid outside of this region $x > L$ is also defined as $h(x, t)$. We consider two particular cases: (a) when the the contact point L is fixed for example a flat indenter with corners, $\eta(x) = 0$, and (b) when the contact point L is moving and the indenter has some geometry $\eta(x)$ for example a cylindrical indenter or a flat indenter with rounded edges. In case (a) we would like to solve for the height the free-surface reaches up the side of the indenter $h(L, t) = h_L(t)$, whereas in case (b) we would like to solve for the contact point $L(t)$ and hence calculate $h_L(t) = \delta(t) + \eta(L)$, see figure 1.

The shallow-layer approximation can be used when the characteristic length scales are much greater than the characteristic height scales, $x_0 \gg h_0$.

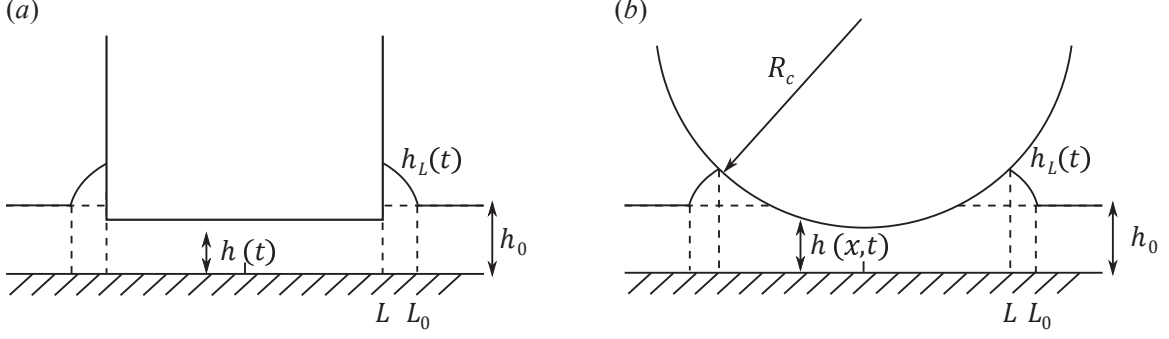


Figure 1: Schematic of (a) flat-based indenter, $\eta(x) = 0$ and (b) cylinder, $\eta(x) = \frac{1}{2R_c}x^2$.

2.2 Bingham rheology

To parametrise the viscoplastic layer we consider a Bingham rheology. A Bingham rheology is one in which the stress tensor varies linearly with strain rate provided the stress is above a given yield stress. Below this yield stress the strain rate is zero. This can be summarised as follows

$$\tau_{ij} = \left(\frac{\tau_Y}{\dot{\gamma}} + \mu \right) \dot{\gamma}_{ij} \quad |\tau| > \tau_Y, \quad (1)$$

$$\dot{\gamma}_{ij} = 0 \quad \text{otherwise,} \quad (2)$$

where $\dot{\gamma} = \sqrt{\frac{1}{2}\dot{\gamma}_{ij}\dot{\gamma}_{ij}}$ and $\tau = \sqrt{\frac{1}{2}\tau_{ij}\tau_{ij}}$. The form of the yield stress τ_Y depends on the rheology of the substrate. For the purely cohesive case, the yield stress is constant and for the non-cohesive case the yield stress varies linearly with pressure, $\tau_Y = p \tan \phi$, where ϕ is the angle of friction.

Assuming horizontal scales x_0 are much larger than vertical scales h_0 , the thin film approximation can be used such that

$$u \gg w \quad \text{and} \quad \frac{\partial}{\partial x} \ll \frac{\partial}{\partial z}. \quad (3)$$

These scales allow $O(\epsilon = h_0/x_0)$ terms to be identified in the momentum equation and the strain rate tensor, and hence gives

$$\frac{\partial}{\partial z} \tau_{xz} = \frac{\partial p}{\partial x}, \quad (4)$$

$$0 = \frac{\partial p}{\partial z} + \rho g. \quad (5)$$

The pressure can then be integrated to give

$$p = P + \rho g(h - z), \quad (6)$$

where P is the pressure at $z = h$. Substituting into the momentum equation then gives the stress as a function of x and z ,

$$\tau_{xz} = T_{xz} + (P_x + \rho g h_x)(z - h) \equiv \left(\frac{\tau_Y}{\dot{\gamma}} + \mu \right) u_z \quad \text{for} \quad |\tau_{xz}| > \tau_Y, \quad (7)$$

where T_{xz} is the stress at $z = h$. The model can be split into two regions: region 1 below the indenter $-L \leq x \leq L$; and region 2 outside the indenter $x \geq L$. In region 1 there are no-slip conditions on the top and bottom boundaries generating a squeeze flow beneath the indenter. In region 2 there is a free-surface on the top boundary giving a zero stress boundary condition there.

2.3 Purely cohesive, $\tau_Y = \text{constant}$

2.3.1 Free-surface flow

For the free-surface flow $T_{xz} = 0$ and $P = 0$ due to the zero normal stress condition on the top surface. From equation (7) in section 2.2 we then have

$$u_z = \frac{(P_x + \rho g h_x)}{\mu} (z - h) - \frac{\text{sgn}(u_z)}{\mu} \tau_Y. \quad (8)$$

The $\text{sgn}(u_z)$ is required because the fluid is yielded when $|\tau| > \tau_Y$. Rearranging the equation for the velocity gradient gives an expression for the yield surface Y when $\dot{\gamma} \equiv |u_z| = 0$,

$$u_z = -\frac{\rho g h_x}{\mu} (Y - z) \quad \text{where} \quad Y = h + \frac{\tau_Y}{\rho g h_x}. \quad (9)$$

Integrating and using the no-slip boundary condition at $z = 0$ gives velocity field

$$u = -\frac{\rho g h_x}{2\mu} (2Y - z)z \quad 0 \leq z \leq Y, \quad (10)$$

$$u = u_p = -\frac{\rho g h_x}{2\mu} Y^2 \quad Y \leq z \leq h, \quad (11)$$

where u_p is the plug velocity. Integrating the free-surface flux and then applying local mass conservation gives a governing equation for the evolution of the free surface

$$\frac{\partial h}{\partial t} = \frac{\rho g}{6\mu} \frac{\partial}{\partial x} (h_x Y^2 (3h - Y)), \quad F^{FS} = -\frac{\rho g h_x}{6\mu} Y^2 (3h - Y), \quad (12)$$

where F^{FS} is the net horizontal flux.

2.3.2 Squeeze flow

Underneath the indenter there is a squeeze flow as fluid is pushed out the way by the indenter. The no-slip boundaries conditions give a parabolic profile suggesting there is a plug region in the centre at the turning point where $u_z = 0$. We can also assume symmetry about the centre line $z = h/2$ and hence apply boundary conditions

$$u = 0 \quad \text{at} \quad z = 0, \quad u_z = 0 \Rightarrow \tau_{xz} = 0 \quad \text{at} \quad z = \frac{h}{2}. \quad (13)$$

The stress can be written as

$$\tau_{xz} = (P_x + \rho g h_x) \left(z - \frac{h}{2} \right) \equiv \left(\frac{\tau_Y}{\dot{\gamma}} + \mu \right) u_z. \quad (14)$$

As in the free-surface case, this can be rearranged to give the velocity gradient in terms of the yield surfaces Y_{\pm} for $z < Y_-$ and $z > Y_+$,

$$u_z = -\frac{\Gamma}{\mu} (Y_{\pm} - z) \quad \text{where} \quad Y_{\pm} = \left(\frac{h}{2} \pm \frac{\tau_Y}{|\Gamma|} \right), \quad (15)$$

and $\Gamma = P_x + \rho g h_x$ is the reduced pressure gradient. The squeeze flow flux can be found by integrating the velocity gradient

$$F_{SF} = 2 \int_0^{\frac{h}{2}} u \, dz \equiv 2 \int_0^{Y_-} \left(\frac{h}{2} - z \right) u_z \, dz = -\frac{\Gamma}{3\mu} Y_-^2 \left(\frac{3h}{2} - Y_- \right). \quad (16)$$

Hence, applying local mass conservation with $h(x, t) = \delta(t) + \eta(x)$, the governing equation for the pressure gradient can be written as

$$x \dot{\delta} = \frac{\Gamma}{3\mu} \left(\frac{h}{2} - \frac{\tau_Y}{|\Gamma|} \right)^2 \left(h + \frac{\tau_Y}{|\Gamma|} \right). \quad (17)$$

2.3.3 Global mass conservation and equation of motion for $\delta(t)$

We consider global conservation of mass to relate the depth δ to contact length L . By considering the area underneath the indenter, global conservation of mass can be written as a sum of integrals in the two regions,

$$h_0 L_0 = \delta L + \int_0^L \eta \, dx + \int_L^{L_0} h^{FS} \, dx, \quad (18)$$

where L_0 is the half-length of the deforming substrate, see figure 1. To close the system, the equation of motion for $\delta(t)$ can be written as,

$$m \ddot{\delta} = -mg + 2 \int_0^L P \, dx, \quad (19)$$

where m is the mass per unit width of the indenter and g is the acceleration due to gravity.

2.3.4 Non-dimensionalisation

We non-dimensionalise vertical and horizontal lengthscales by the initial depth of fluid h_0 and characteristic lengthscale of the geometry x_0 respectively. A scale for the pressure is defined by balancing the normal force due to the fluid with the weight of the indenter. Finally, a timescale is defined by balancing the inertial forcing with the weight of the indenter. Hence, non-dimensional variables can be defined as,

$$\hat{x} = \frac{x}{x_0}, \quad \hat{h} = \frac{h}{h_0}, \quad \hat{P} = \frac{P}{P_0} = \frac{x_0}{mg} P, \quad \hat{t} = \frac{t}{t_0} = \left(\frac{g}{h_0} \right)^{1/2} t. \quad (20)$$

Dropping the hat decoration, the governing equations for the free-surface flow, the squeeze flow and the evolution of $\delta(t)$ then reduce to

$$V \frac{\partial h}{\partial t} = \frac{R}{6} \frac{\partial}{\partial x} (h_x Y^2 (3h - Y)) \quad \text{with} \quad Y = h + \frac{B}{Rh_x} \quad (21)$$

$$Vx\dot{\delta} = \frac{\Gamma}{3} \left(\frac{h}{2} - \frac{B}{|\Gamma|} \right)^2 \left(h + \frac{B}{|\Gamma|} \right), \quad (22)$$

$$L_0 = \delta L + \int_0^L \eta dx + \int_L^{L_0} h^{FS} dx \quad (23)$$

$$\ddot{\delta} = -1 + 2 \int_0^L P dx, \quad (24)$$

with parameters

$$B = \tau_Y x_0^2 / mgh_0, \quad R = \rho x_0 h_0 / m, \quad \text{and} \quad V = \mu x_0^3 / mh_0^2 \sqrt{gh_0}. \quad (25)$$

The Bingham number B characterises the strength of the substrate, R controls the influence of gravity and V the influence of viscosity. This model is valid until $\dot{\delta} = 0$ at which point the squeeze flow turns off and the layer plugs up.

2.3.5 Plastic limit, free-surface

In the plastic limit, as $V \rightarrow 0$, the terms involving time dependence in the free-surface and squeeze evolution equations are small and hence the flow becomes quasi-static. For the free-surface flow this implies $Y = h + B/Rh_x \rightarrow 0$, hence

$$hh_x = -\frac{B}{R} \quad \Rightarrow \quad h = \left(h_L^2 + \frac{2B}{R}(L-x) \right)^{1/2}. \quad (26)$$

2.3.6 Plastic limit, squeeze flow case (a): flat-based indenter, $\eta(x) = 0, x_0 = L$

In the plastic limit, the yield surfaces $Y_{\pm} = h/2 \mp B/(P_x + Rh_x)$ in the squeeze flow also tend to the boundaries, $Y_- \rightarrow 0, Y_+ \rightarrow h$ implying

$$\frac{h}{2} = -\frac{B}{P_x + Rh_x}. \quad (27)$$

Assuming further that $R \ll 1$ so the hydrostatic pressure is small, the pressure in the squeeze flow can be solved for with boundary condition $P(x=1) = R(h_L - \delta) \ll 1$,

$$P_x = -\frac{2B}{\delta} \quad \Rightarrow \quad P = \frac{2B}{\delta}(1-x). \quad (28)$$

Substituting the pressure into the evolution equation for δ we have,

$$\ddot{\delta} = -1 + \frac{4B}{\delta} \int_0^1 (1-x) dx = -1 + \frac{2B}{\delta}, \quad (29)$$

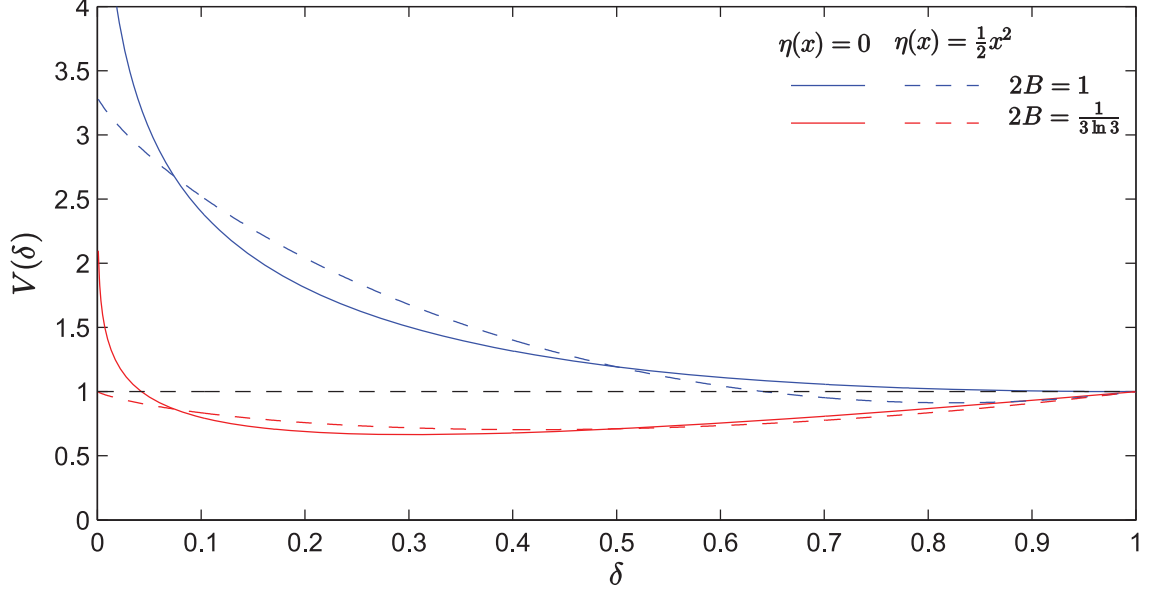


Figure 2: Potential energy $V(\delta)$ against depth δ for the flat-based indenter (solid lines) and the parabolic indenter (dashed lines) and two values of the Bingham number $2B = 1, 1/3 \ln 3$ given by the blue and red lines, respectively.

which defines equilibrium depth $\delta_{eq} = 2B$ where the normal force due to the fluid balances the weight of the object. Multiplying by $\dot{\delta}$ the energy equation can be derived, and hence an expression for the final depth of the indenter δ_f ,

$$1 + \frac{\dot{\delta}_0^2}{2} = V(\delta_f) = \delta_f - 2B \ln \delta_f. \quad (30)$$

The minimum value of $V(\delta)$ is attained at the equilibrium depth $\delta = \delta_{eq} = 2B$, with value $V(\delta_{eq}) = 2B - 2B \ln 2B$. When $\dot{\delta}_0 = 0$ and $2B < 1$ ($\delta_{eq} < 1$), the indenter sinks to a height δ_f . However, when $\dot{\delta}_0 = 0$ and $2B > 1$, the equilibrium depth is above the height of the layer. This is because the layer is not sufficiently stressed to deform so the indenter remains on the surface with $\delta_f = 1$, see figure 2.

2.3.7 Plastic limit, squeeze flow case (b): parabola $\eta(x) = \frac{1}{2}x^2, x_0 = (R_c h_0)^{1/2}$

In the case of a parabolic indenter (local approximation for a cylinder), the pressure gradient can be written as,

$$P_x = -Rx - \frac{2B}{\delta \left(1 + \frac{1}{2\delta}x^2\right)}. \quad (31)$$

The normal force due to the fluid is given by

$$2 \int_0^L P dx = -2 \int_0^L x P_x dx = 2 \int_0^L Rx^2 + \frac{2Bx}{\delta \left(1 + \frac{1}{2\delta}x^2\right)} dx = \frac{2RL^3}{3} + 4B \ln \left(1 + \frac{1}{2\delta}L^2\right). \quad (32)$$

Unlike the flat-based indenter with fixed L , for the parabola the evolution of $\delta(t)$ is coupled to the evolution of $L(t)$. Global conservation of mass gives

$$\frac{L^3}{6} - L(1 - \delta) + \frac{R}{6B}(2h_L + 1)(h_L - 1)^2 = 0. \quad (33)$$

In the limit of $R \ll 1$, the conservation of volume reduces to $L^2 = 6(1 - \delta)$, hence the energy equation for δ can be written as

$$\frac{\dot{\delta}_0^2}{2} + 1 = V(\delta) = \delta_f + 4B \left(\frac{1}{2}(3 - 2\delta_f) \ln(3 - 2\delta_f) + \delta_f \ln \delta_f \right). \quad (34)$$

Figure 2 plots the potential energy $V(\delta)$ against the depth of the indenter. The minimum point is given by $\delta = \delta_{eq} = 3/(\exp(1/4B) + 2)$ which tends to 1 as the Bingham number diverges. For $\dot{\delta}_0 = 0$, the parabola appears to reach the bottom provided $2B < 1/3 \ln 3$. In general, equation (34) suggests the parabola reaches the bottom of the initial layer provided the initial speed of the indenter is sufficiently large,

$$\dot{\delta}_0^2 > 2(6B \ln 3 - 1). \quad (35)$$

However, in the plastic limit there will always be a thin viscous layer between the parabola and the base of the substrate. This is violated in this case because the assumption that the yield surfaces tend towards the boundaries, $Y_- \rightarrow 0$, $Y_+ \rightarrow h$, breaks down as $\delta \rightarrow 0$. If we rescale the variables in terms of δ , $\hat{x} = x/\delta^{1/2}$, $\hat{h} = h/\delta$, for $\eta(x) = \eta_0 x^n$, then we have

$$V \delta^{\frac{1}{n} - \frac{3}{2}} \dot{\delta} = \frac{\Gamma}{3} \left(\frac{h}{2} - \frac{B}{|\Gamma|} \right)^2 \left(h + \frac{B}{|\Gamma|} \right). \quad (36)$$

For $n > 0$ the left hand side diverges as $\delta \rightarrow 0$ suggesting we are no longer in the quasistatic limit so the approximation of $Y_- \rightarrow 0$, $Y_+ \rightarrow h$ is not valid. Hence, equation (34) does not hold for small δ .

2.4 Numerical solution

The full system described by equations (21–24) can be solved numerically using MATLAB's in-built solver ODE15s. Figure 3 shows the numerical solution for parameters $V = 1, B = 1$ and $R = 1$ with initial condition $\dot{\delta}_0 = -2$. Figure 3(a-c) shows the position of the cylinder, yield surfaces and free-surface profile at time intervals $t = 0.02, 0.14$ and 0.26 . Figure 3(d) plots depth of the cylinder $\delta(t)$ with time to its stopping position at $\delta_f = 0.71, t = 0.29$. In figure 3(a-c) there appears to be a discontinuity between the squeeze flow and free-surface flow as indicated by the transition from two yield surfaces to one. This is because there is an $O(1)$ aspect ratio region at the contact line $x = L$ which is not captured by the lubrication model, where the yielded and plug regions smoothly transition. Instead the lubrication model matches the two regions by taking the horizontal volume flux to be continuous at $x = L$.

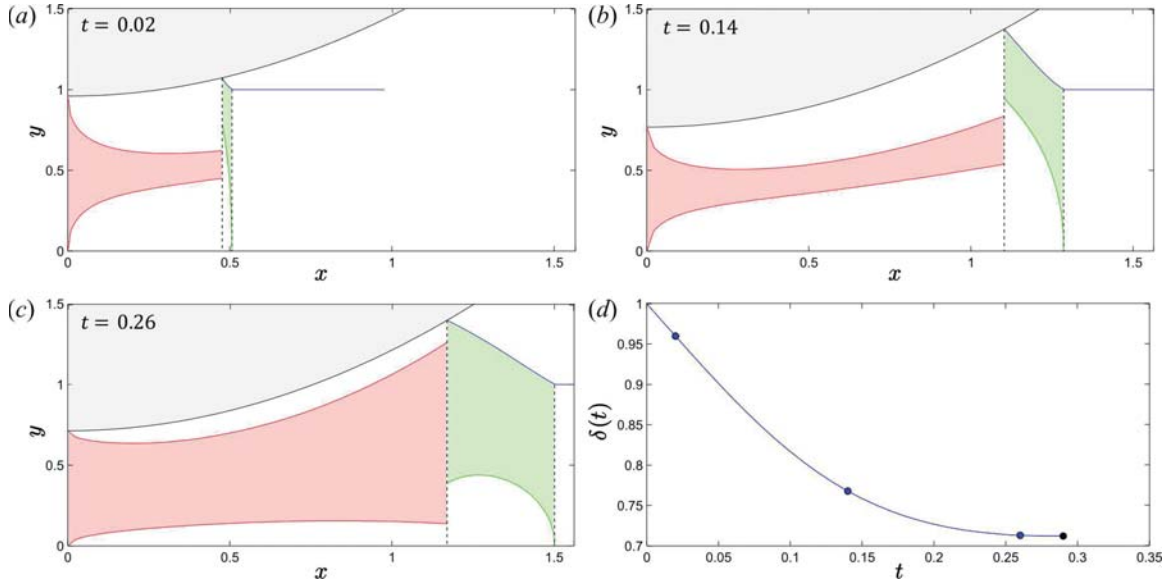


Figure 3: Full numerical solution for a parabolic indenter dropped onto a pure cohesive substrate with $\dot{\delta}_0 = -2$, $V = 1$, $B = 1$ and $R = 1$ plotted at (a) $t = 0.02$, (b) $t = 0.14$, and (c) $t = 0.26$. The coloured lines indicate the edge of cylinder (black), free surface (blue), yield surfaces in the squeeze flow (red), and yield surfaces in free surface flow (green), with black dashed lines separating the squeeze flow and the free-surface flow. The squeeze flow plug, free-surface plug and cylinder are shaded in red, green and grey, respectively. (d) Height of the cylinder with time. Blue dots are plots are $t = 0.02, 0.14, 0.26$ and the black dot is final resting place of cylinder when $\dot{\delta} = 0$ at $\delta_f = 0.71$, $t = 0.29$.

2.5 Mohr-Coulomb $\tau_Y = p \tan \phi$

In a Mohr-Coulomb model, the stress tensor can be written as

$$\tau_{ij} = \tau_Y \frac{\dot{\gamma}_{ij}}{\dot{\gamma}} \quad \text{where} \quad \tau_Y = c + p \tan \phi, \quad (37)$$

where c is the cohesion and ϕ is the internal friction angle. For generality, we will consider $c \neq 0$ to begin with and then take $c = 0$ for the non-cohesive case. As in the Bingham model, we regularise by adding a viscous term in order to solve for the flow field. This gives

$$\tau_{ij} = \left(\frac{c + p \tan \phi}{\dot{\gamma}} + \mu \right) \dot{\gamma}_{ij}. \quad (38)$$

2.5.1 Free-surface flow

For the free surface flow $p(z = h) = 0$, which gives

$$\mu u = (-\rho g h h_x - c - \rho g h \tan \phi) z + \frac{1}{2} (\rho g h_x + \rho g \tan \phi) z^2. \quad (39)$$

Setting $u_z = 0$ defines the yield surfaces

$$Y = h - \frac{c}{\rho g (|h_x| - \tan \phi)}. \quad (40)$$

As in the pure cohesive case, the governing equation for h can be found by considering local mass conservation to give

$$\frac{\partial h}{\partial t} = \frac{\partial}{\partial x} \left(\frac{\rho g (h_x + \tan \phi)}{6\mu} Y^2 (3h - Y) \right). \quad (41)$$

2.5.2 Squeeze flow

The squeeze flow is treated in a similar manner to the pure cohesive case. In the bottom yielded region, the velocity gradient can be integrated to give the velocity for $0 < z < Y_-$

$$\mu u_z = \Gamma (z - Y_-) + \rho g \tan \phi (z - Y_-) \quad \Rightarrow \quad \mu u_- = (\Gamma + \rho g \tan \phi) z \left(\frac{z}{2} - Y_- \right), \quad (42)$$

where $\Gamma = P_x + \rho g h_x$. Similarly, the velocity in the top yielded region for $Y_+ < z < h$ can be written as

$$\mu u_+ = (\Gamma - \rho g \tan \phi) \left[z \left(\frac{z}{2} - Y_+ \right) - h \left(\frac{h}{2} - Y_+ \right) \right]. \quad (43)$$

One equation for the yield surfaces is given by matching the plug speeds, $u_-(Y_-) = u_+(Y_+)$,

$$h - \left(\frac{-\Gamma - \rho g \tan \phi}{-\Gamma + \rho g \tan \phi} \right)^{1/2} Y_- = Y_+. \quad (44)$$

Another equation is given by setting the top and bottom boundaries to be at the yield stress

$$-\Gamma (Y_+ - Y_-) = 2c + 2P \tan \phi + \rho g \tan \phi (2h - Y_- - Y_+). \quad (45)$$

Depth integrating the velocity and applying local mass conservation an ODE for the pressure P can be found,

$$-x \dot{\delta} = \frac{(\Gamma + \rho g \tan \phi)}{6\mu} Y_-^3 - \frac{(\Gamma - \rho g \tan \phi)}{6\mu} (Y_+^3 - 3Y_+ h^2 + 2h^3). \quad (46)$$

2.5.3 Non-dimensionalisation

We non-dimensionalise as in section 2.3.4 which gives the additional non-dimensional parameter $\Phi = \frac{x_0}{h_0} \tan \phi$ which controls the influence of the angle of friction ϕ . The Bingham number is now written as $B = cx_0^2/mgh_0$.

2.5.4 Plastic limit, free-surface

In the plastic limit, $Y \rightarrow 0$, and equation for the quasistatic free surface $h(x, t)$ can be found

$$\frac{hh_x}{\frac{B}{R\Phi} + h} = -\Phi, \quad (47)$$

Using boundary condition $h(L, t) = h_L$, this can be integrated to give

$$h - h_L - \frac{B}{R\Phi} \ln \left(\frac{h + \frac{B}{R\Phi}}{h_L + \frac{B}{R\Phi}} \right) = (L - x)\Phi. \quad (48)$$

In the non-cohesive case, $B = 0$, the free surface profile in the plastic limit reduces to the linear profile with gradient given by the angle of friction ϕ ,

$$h - h_L = (L - x)\Phi. \quad (49)$$

2.5.5 Plastic limit, squeeze flow case (a): flat-based indenter $\eta(x) = 0, x_0 = L$

In the plastic limit, the yield surfaces tend to the boundaries, $Y_- \rightarrow 0, Y_+ \rightarrow h = \delta(t)$. Hence, this gives

$$-P_x \delta = 2B + 2\Phi P + R\Phi \delta. \quad (50)$$

Multiplying by an integrating factor and using boundary condition $P(x = 1) = R(h_L - \delta)$, an expression for the pressure can be found

$$P = - \left(\frac{B}{\Phi} + \frac{R\delta}{2} \right) + \left(Rh_L - \frac{R\delta}{2} + \frac{B}{\Phi} \right) \exp \left(\frac{2\Phi}{\delta} (1 - x) \right) \quad (51)$$

The equation of motion for the depth of the indenter in the non-cohesive case is then given by

$$\ddot{\delta} = -1 - R\delta - \frac{\delta}{\Phi} \left(Rh_L - \frac{R\delta}{2} \right) \left(1 - \exp \left(\frac{2\Phi}{\delta} \right) \right). \quad (52)$$

A relationship between h_L and δ is found by considering global mass conservation

$$1 - \delta = \frac{1}{2}(h_L - 1)(L_0 - 1) \Rightarrow h_L = 1 + (2\Phi(1 - \delta))^{1/2}. \quad (53)$$

The force balance equation can then be integrated to give an expression for δ_f in terms of initial condition $\dot{\delta}_0$ and parameters Φ and R ,

$$1 + \frac{\dot{\delta}_0^2}{2} = \delta_f + R \int_{\delta_0}^{\delta_f} \left(\delta + \delta \left(\left(\frac{2(1 - \delta)}{\Phi} \right)^{1/2} - \frac{\delta}{2\Phi} \right) \left(1 - \exp \left(\frac{2\Phi}{\delta} \right) \right) \right) d\delta. \quad (54)$$

Figure 4 plots the final depth δ_f as a function of Φ and R (blue and red solid lines). For small $1/R$, the flat-based indenter sits on the surface of the plastic layer with $\delta_f = 1$. As in the pure cohesive case, this defines a yield criterion as a function of parameters Φ and R where the layer is not sufficiently stressed to deform.

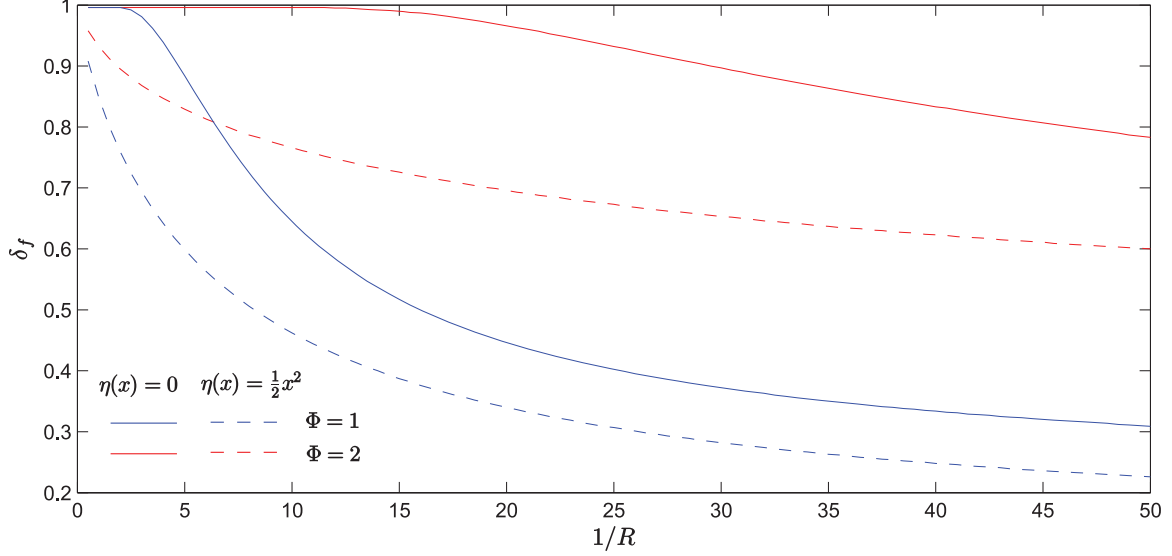


Figure 4: Plot of the final depth δ_f as a function of $1/R$ for a flat-based indenter (solid lines) and parabolic indenter (dashed lines) with $\Phi \in \{1, 2\}$.

2.5.6 Plastic limit, squeeze flow case (b): parabola $\eta(x) = \frac{1}{2}x^2$, $x_0 = (R_c h_0)^{1/2}$

For a parabolic indenter, $h = \delta(t) + \frac{1}{2}x^2$, the pressure in the squeeze flow is given by $\Gamma = P_x + Rx$. Hence, in the plastic limit

$$-(P_x + Rx) \left(\delta + \frac{1}{2}x^2 \right) = 2B + 2\Phi P + R\Phi \left(\delta + \frac{1}{2}x^2 \right). \quad (55)$$

In the non-cohesive case,

$$P_x + \frac{2\Phi P}{\delta + \frac{1}{2}x^2} = -R(x + \Phi). \quad (56)$$

This can be integrated with boundary condition $P(x = L) = R(h_L - \delta)$. Substituting the pressure into the force balance equation, together with global mass conservation

$$\left(\delta + \frac{1}{2}L^2 - 1 \right)^2 = 2\Phi \left(L(1 - \delta) - \frac{1}{6}L^3 \right), \quad (57)$$

and integrating twice, an expression for δ_f can be found in terms of $\dot{\delta}_0$ and parameters Φ and R , see section 2.5.5. Figure 4 plots the final depth δ_f as a function of Φ and R (blue and red dashed lines).

2.6 Deep plastic layer

Thus far we have considered a shallow layer of viscoplastic fluid in order to understand the deformation of a shallow plastic layer. The case of a deep layer has been studied extensively using the method of characteristics [14, 9]. These studies calculate the pressure

underneath a flat-based indenter placed onto a rigid-plastic half-space by the construction of sliplines. We outline here the method for constructing sliplines and state two key results for a purely cohesive and a non-cohesive substrate. We then describe three possibilities for the free-surface displacement.

In the deep layer limit, we require the full force-balance equations

$$\frac{\partial \sigma_z}{\partial x} + \frac{\partial \tau_{xz}}{\partial z} = 0, \quad \frac{\partial \sigma_x}{\partial z} + \frac{\partial \tau_{xz}}{\partial x} = 0, \quad (58)$$

where σ_x and σ_z are the normal stress components in the x and z directions respectively and τ_{xz} is the shear stress. Requiring yield condition $(\sigma_x - \sigma_z)^2 + 4\tau_{xz}^2 = 4\tau_Y^2$, the stress components can then be written in terms of new parameter θ ,

$$\sigma_x = -p + \tau_Y \sin 2\theta, \quad \sigma_z = -p = -\tau_Y \sin 2\theta \quad \text{and} \quad \tau_{xz} = \tau_Y \cos 2\theta. \quad (59)$$

Substituting the parametrisation (59) into the full force-balance equations (58) and differentiating, equations for p and θ can be found

$$\left(\cos \theta \frac{\partial}{\partial x} + \sin \theta \frac{\partial}{\partial z} \right) (p + 2\tau_Y \theta) = \left(\sin \theta \frac{\partial}{\partial x} - \cos \theta \frac{\partial}{\partial z} \right) (p - 2\tau_Y \theta) = 0. \quad (60)$$

These define two sets of characteristics (α and β characteristics) along which quantities $p \pm 2\tau_Y \theta$ are conserved. To solve for the slipline field the quantities p and θ first need to be defined along some boundary. The values of p and θ are calculated elsewhere by integrating along the characteristics equations (60) from a region of known information.

For the case of a pure cohesive plastic layer where $\tau_Y = \text{constant}$, the pressure underneath an indenter of contact length $a = 2L$ can be calculated analytically and is given by

$$p = \tau_Y(2 + \pi), \quad (61)$$

[14]. The force per unit length is therefore $F = \tau_Y(2 + \pi)a$. For the case of a non-cohesive material such that $\tau_Y = p \tan \phi$, the pressure is given by

$$p = \frac{1}{2} \rho g N_\gamma a, \quad (62)$$

where $N_\gamma = 6.5$ is a Terzaghi coefficient [19, 3] calculated numerically, with force per unit length $F = \frac{1}{2} \rho g N_\gamma a^2$. These expressions for the force F describe the initial condition where a flat-based indenter of contact length a is placed onto the flat surface of a deep plastic layer. Hence, this theory can only be extended to small deformations of the layer where the surface can be approximated as horizontal.

For a flat-based indenter, comparing the weight of the indenter with the force exerted by the plastic layer gives a yield criterion for when the indenter can deform the substrate. For example in the pure cohesive case, the indenter will deform the substrate provided

$$\tau_Y \leq \frac{mg}{(2 + \pi)wa}, \quad (63)$$

where m and w are the mass and length of the indenter, respectively. To determine the equilibrium depth of the indenter, the velocity field must be calculated to update the free

surface, and hence calculate the new force exerted by the plastic layer. An iterative numerical approach can then be used to determine the depth at which the forces are in balance.

For the case of a parabolic indenter, the increasing contact length with depth of indentation means more progress can be made analytically. Again, for the pure cohesive case, equating the force exerted by the plastic layer with the weight of the indenter gives a contact length $a = mg/\tau_Y(2 + \pi)w$. The contact length must now be related to the depth of the indentation. Figure 5 shows possible relationships between contact length a and depth of indentation d . Figure 5(a) shows when the layer is allowed to compact such that there is no free-surface deformation, in contrast to the previous formulation where we assumed incompressibility. As a result the free surface remains horizontal with $d = \frac{1}{2R_c}(a/2)^2$ for shallow depths d . In figure 5(c) we have considered when gravity is neglected giving a vertical free-surface. Conservation of mass then implies $d = \frac{1}{6R_c}(a/2)^2$. We anticipate the free-surface to be in between these two end-members such as figure 5(b). For the pure cohesive case, the free-surface displacement for shallow indentations can be found using the slipline calculations [18]. For small deformations due to the curved surface of a cylinder, the velocity on the surface of the plastic layer is shown to be

$$v(x, t) = \begin{cases} -V & 0 \leq x \leq a/2 \\ V & a/2 \leq x \leq a, \end{cases} \quad (64)$$

where the length of the deformed region outside is the same as the half-length of the indenter due to the symmetry of the slipline field. And hence, the deformed region outside has profile [18]

$$h = d - \frac{x^2}{14R_c} \quad \text{where} \quad d = \frac{2}{7R_c} \left(\frac{a}{2}\right)^2. \quad (65)$$

For the parabolic indenter, the contact length and depth as function of the mass of the indenter are therefore given by

$$a = \frac{mg}{\tau_Y(2 + \pi)w}, \quad d = \frac{1}{14R_c} \left(\frac{mg}{\tau_Y(2 + \pi)w}\right)^2, \quad (66)$$

for a pure cohesive substrate, and

$$a = \left(\frac{2m}{\rho N_\gamma w}\right)^{1/2}, \quad d = \frac{2m}{14R_c \rho N_\gamma w}, \quad (67)$$

for a Mohr-Coulomb substrate.

In this section we have described a theoretical model for the loading stage of indentation where either a flat-based or parabolic indenter is placed onto a shallow plastic layer. We have also outlined the current theory for indentation of a deep plastic layer using the method of characteristics to build up a slipline field. In the next section we will describe experiments of indentation into shallow and deep layers with the aim of making comparisons with the theory described.

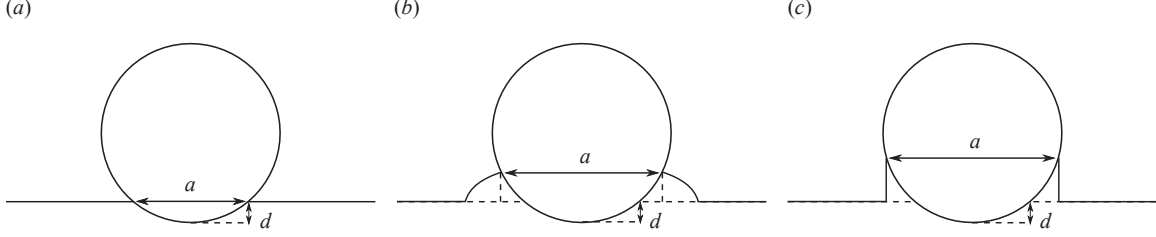


Figure 5: Schematic showing possible relationships between contact length a and depth indented into the plastic layer d . (a) Pure compaction $d = \frac{1}{2R_c}(a/2)^2$, (b) some deformation outside $\frac{1}{6R_c}(a/2)^2 < d < \frac{1}{2R_c}(a/2)^2$, and (c) vertical free surface $d = \frac{1}{6R_c}(a/2)^2$.

3 Experiments

3.1 Setup

Experiments were conducted to investigate the relationship between depth, contact length and mass for a cylinder indenting a deformable substrate. Joint compound was used as a Bingham rheology and two sizes of ballotini (0.2mm and 1mm) were used as Mohr-Coulomb rheologies, both with angle of friction $\phi = 24.9 \pm 0.7$. The experimental setup is shown in figure 6. A clear perspex cylinder of radius $R_c = 0.076$ m was attached to the end of a lever that was allowed to rotate about a pivot. Weights were placed on the lever and incrementally moved along to increase the moment, and hence mass on the cylinder. A scale placed on the inside of the cylinder allowed the contact arc length to be measured by eye. Two cameras were also set up to record the displacement of the cylinder. The first camera took photos parallel to the substrate surface to measure the depth of the cylinder, figure 6(b). The second camera was placed at a known oblique angle to take photos of a laser line shone through the cylinder, figure 6(c). This gave a second measurement of the contact arc length and depth as well as a profile of the free surface outside.

3.2 Image processing

Photographs taken parallel to the substrate were analysed to determine the depth of the indentation. A blue strip on the top of the cylinder was used to track the displacement between images. We found that the cylinder compressed slightly due to the weight placed on top. As a result, a compliance test was carried out to measure the deformation of the cylinder under a given load when placed on a rigid surface. This is then subtracted from the measured displacements.

Photographs of the laser line taken at known oblique angle were analysed to deduce the profiles of the indentations, see figure 7(a). Firstly, the red filter of the image is taken to get an intensity plot figure 7(b). A moving average is then used to smooth the profiles, with a lower threshold chosen to eliminate noise. The profile is then determined by calculating the weighted average along each vertical strip of pixels, figure 7(c) (blue solid line). The laser line was imaged through the bottom half of the cylinder causing some distortion of the profile to take place. This is corrected for by subtracting off a reference profile of the

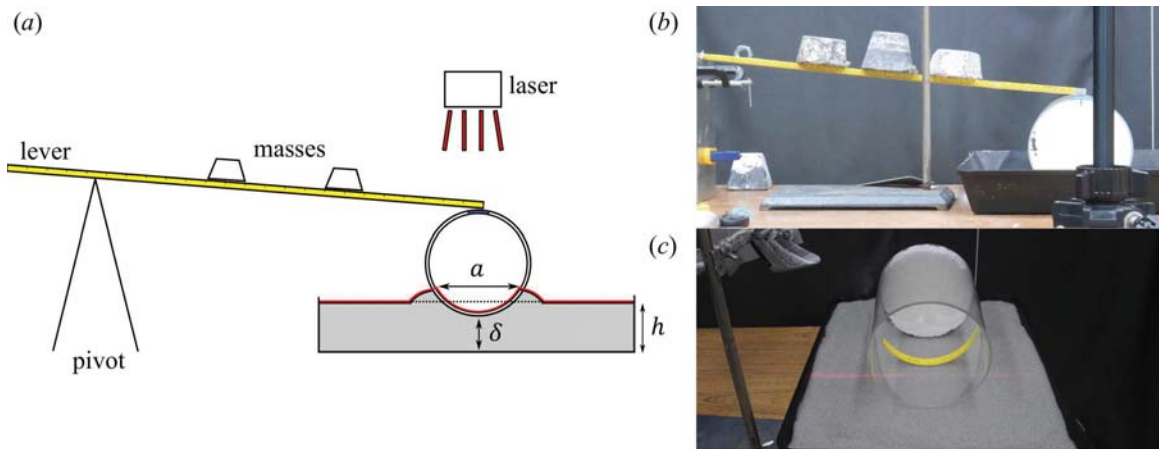


Figure 6: Experimental setup. (a) Schematic of the experimental setup. (b) Sample photograph taken from the first camera parallel to the substrate, and (c) taken from the second camera at known oblique angle.

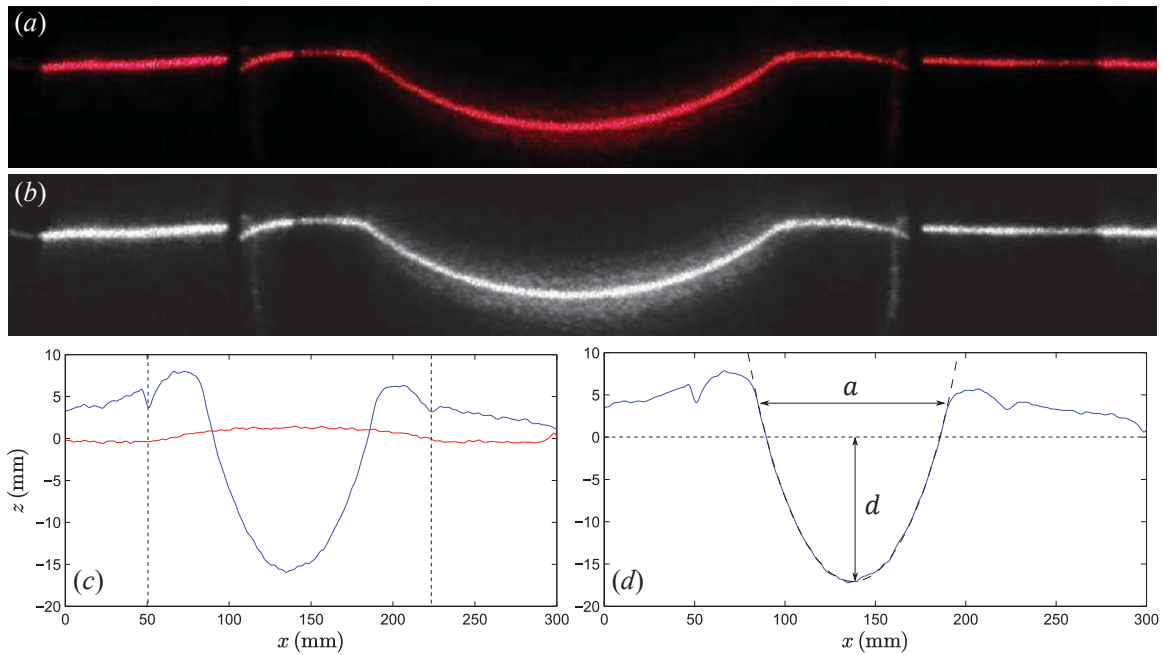


Figure 7: Image processing for joint compound experiment with $h_0 = 4$ cm. (a) Image of laser line, and (b) red filtered image of laser line. (c) Detected displacement of joint compound (blue solid line) and reference profile of laser line projected through the perspex cylinder (red solid line), edge of the cylinder indicated by vertical black-dashed lines. (d) Final profile of displacement.

cylinder resting on the surface of the joint compound with no mass, figure 7(c) (red solid line), where the black-dashed lines indicate the edge of the cylinder. The final displacement profile is given in figure 7(d) with the contact length a and the depth d indicated and superimposed cylinder outline given by the black dashed line.

3.3 Joint Compound

3.3.1 Yield stress

A slump test can be used to measure the yield stress of the joint compound. From section 2.3.5, the final profile of a shallow slump of plastic fluid is given by

$$h(x) = \left(\frac{2\tau_Y}{\rho g} (L_s - x) \right)^{1/2} \quad (68)$$

where L_s is the radius of the slump, [10]. By measuring the radius and central height of a slump of joint compound, the yield stress can be measured, $\tau_Y = \rho g h_0^2 / 2L_s$. In our experiments, the yield stress is measured to be $\tau_Y = 35 \pm 5$ Pa.

3.3.2 Loading experiments

For the joint compound, we carried out a series of loading experiments where the mass on the cylinder was gradually increased by moving masses along the pivot lever. The depth, δ_f , and contact length, $a = 2L$, where measured using the methods described in section 3.1. Figure 8 plots the depth and contact length against the applied mass for four different substrate heights $h_0 = 1, 2, 3$ and 4cm. Figure 8(b) shows excellent agreement between the contact length measured from the profiles (filled circles) and the contact length measured by eye (empty squares). As the depth of the substrate increases, the contact lengths begin to collapse onto a universal curve, seen by the close agreement between the contact lengths for $h_0 = 3$ cm (orange points) and $h_0 = 4$ cm (purple points). This is to be expected since as h_0 increases there is a transition from indenting a shallow layer where the depth δ_f is proportional to h_0 to indenting a deep layer where the depth δ_f is independent of h_0 . Figure 8(a) plots the depth against applied mass and shows there is a discrepancy between the depth measured from the profiles (filled circles) and the depth measured from tracking the side view of the cylinder (empty squares). The depth measured from the profiles show a collapse of the data for larger substrate depths onto a universal curve (orange and purple filled circles), consistent with the measured contact length, whereas the depth measured from the side profiles show a continued increase in depth. In addition, the profiles seen in figures 7, 9 are in excellent agreement with the theoretical cylinder shape with measured radius $R_c = 0.076$ m (black dashed lines) suggesting there is no error in converting the profiles to depths. And hence, the laser line gives a more accurate measure of the depth of the indentation. On possible reason the depth calculated from the side images disagrees could be that the compliance of the cylinder is not properly accounted for. In future experiments, more tests need to be carried out to characterise the compliance of the indenter.

Figure 8 also plots the theoretical curves for the deep plastic layer (black dashed lines) and the viscoplastic layer (black dot-dashed lines). The deep theory is given by equation (66)

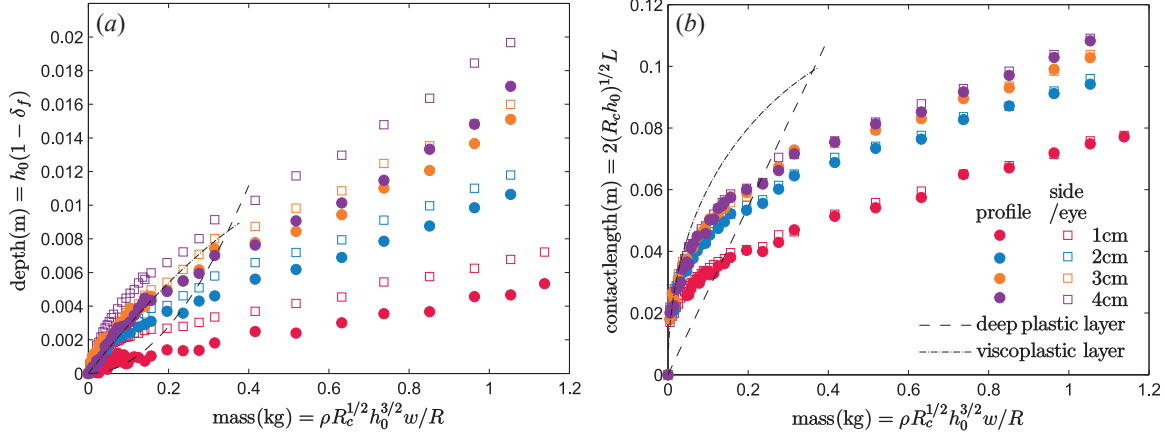


Figure 8: Loading experiments for a cylinder indenting a layer of joint compound. (a) Depth with mass measured using the detected profiles (filled circles) and the photographs tracking the cylinder from side view (empty squares). (b) Contact length with mass measured using the detected profiles (filled circles) and by eye (empty squares). The theoretical curves for the deep plastic layer (black dashed lines) and the viscoplastic layer (black dot-dashed lines) are plotted for parameters $\tau_Y = 35$ Pa, $\rho = 1517$ kgm $^{-3}$, $h_0 = 0.01$ m, $R_c = 0.076$ m and $w = 0.2$ m.

and the viscoplastic theory by numerically solving the force balance outlined in section 2.3.7 with R non-negligible. Qualitatively, the experimental data has the same characteristic shape as suggested by the shallow viscoplastic theory but appears to disagree quantitatively by a scale factor. In terms of the deep plastic theory, initially the contact length appears to grow linearly as suggested by the theory but then quickly diverges. This may be because the surface of the layer can no longer be approximated as horizontal.

3.3.3 Profiles

The detected free-surface profiles can also be used to compare with the theoretical models. Figure 9(a-d) plots the profiles for layer depths $h_0 = 1, 2, 3$ and 4 cm due to applied loads $m = 0.24, 1.05$ kg. For the smallest depth, figure 9(a), the theoretical curve (26) is plotted for two values of the yield stress $\tau_Y = 20$ and 35 Pa and suggests a smaller yield stress than measured from the slump test is required to fit the experimental results. As the layer depth increases, the region over which deformation occurs increases. For the largest layer depth, figure 9(d), the deformation begins to reach the edge of the containing box. As a result, the flow can feel the influence of the side walls and hence mobilises a larger region of the layer than suggested by the theoretical free-surface for the deep plastic layer (green solid line). In addition, the profiles of layer depth $h_0 = 3$ and 4 cm suggest that mass is not conserved. This could be due to an error zeroing the profiles with the reference image or fluid escaping the test region. To experimentally increase the height of the layer depth, blocks were added into the box to dam a smaller region. Any fluid escaping this region would cause an apparent loss of mass with indentation.

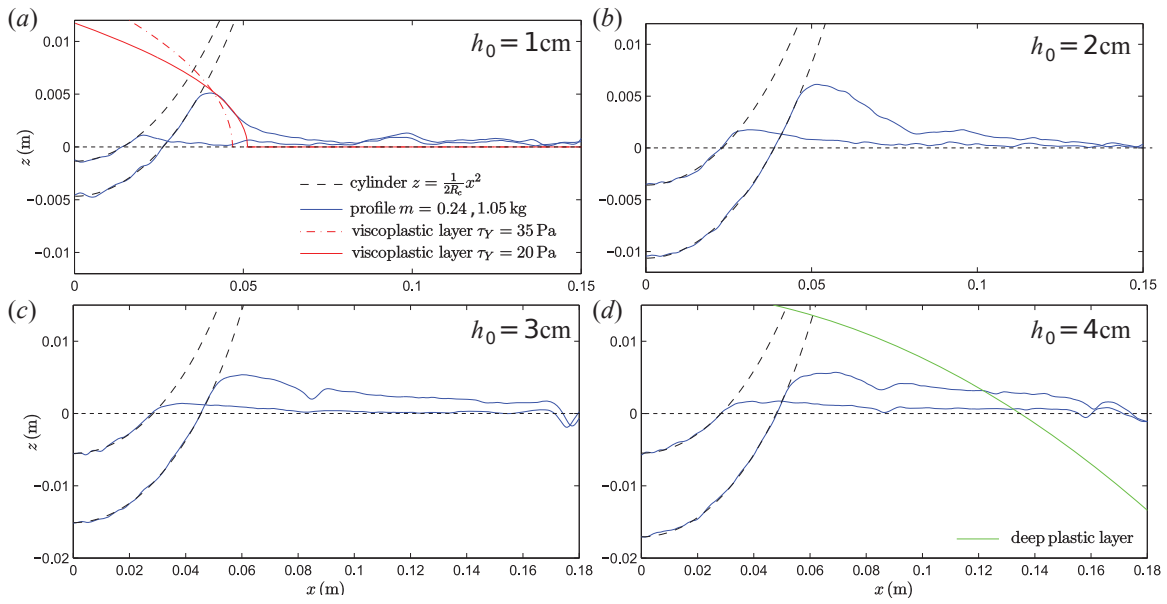


Figure 9: Profiles of loading experiments for a cylinder indenting joint compound for layer depths $h_0 = 1, 2, 3$ and 4 cm, (a-d) respectively, and applied load $m = 0.24, 1.05$ kg (blue lines). (Note change of axes.) Position of the cylinder given by the black dashed lines. (a) Theoretical curves for a viscoplastic free-surface flow with yield stress $\tau_Y = 35$ Pa (red dot-dashed line) and $\tau_Y = 20$ Pa (red solid line). (d) Theoretical curve for a deep plastic layer free-surface profile (green solid line).

3.4 Ballotini

3.4.1 Loading experiments

For the ballotini we again carried out a series of loading experiments for a range of substrate heights $h_0 = 1 - 5\text{cm}$ with ballotini diameters 0.2mm (small) and 1mm (large). Figure 10 plots the depth and contact length against the applied mass, where filled data points indicate large ballotini and empty data points small ballotini. As in the joint compound case, there is a clear difference between shallow and deep substrate depths with the depth of indentation and contact length smaller for $h_0 = 1\text{cm}$ (purple points). This again highlights the transition from indenting a shallow layer to a deep layer. There also appears to be a discrepancy between the small and large ballotini with the same angle of friction ϕ . At the start of each experiment the ballotini substrate was mixed around then levelled once to give a uniform h_0 with a loose structure. This may have led to a different packing density for the two ballotini sizes. For example, if the small ballotini had a tighter packing density we would anticipate the depth of indentation to be less for a given mass. This could explain the difference between the two ballotini sizes however further experiments need to be carried out to rule out other possibilities.

The theoretical curves for the deep plastic layer (black dashed lines) and the viscoplastic layer (black dot-dashed lines) are also plotted on figure 10. The deep plastic layer, see equation (67), does a good job at replicating the linear and square root structure of the depth and contact length for larger substrate depths, whilst the theory for a viscoplastic layer, numerical solution in section 2.5.6, as in the joint compound case, over predicts the depth and contact length for a given mass quantitatively by a scale factor.

3.4.2 Dropping experiments

In addition to the static loading experiments, we carried out a series of dropping experiments to investigate the effect the initial speed of the indenter on the surface of the substrate $\dot{\delta}_0$ has on the final depth δ_f . To do so we dropped the cylinder from a range of increasing heights with the same loading mass each time onto a substrate of 1mm ballotini of depth $h_0 = 5\text{cm}$. Figure 11 shows the final profile for four different heights. This demonstrates that the final depth δ_f increases with initial speed, as anticipated from our formulation in section 2.1.

In this section we have described some preliminary experiments conducted to investigate the indentation of two substrate rheologies with a clear transition between shallow layers, where the indentation is predicted to be proportional to h_0 , and deep layers, where the indentation is predicted to be independent of h_0 . In addition, for the experiments with ballotini, we saw a difference with diameter size suggesting the experiments were very sensitive to initial conditions. For both the ballotini and the joint compound, there is good agreement with the overall shape suggested by the theoretical models however there appears to be a scale factor discrepancy between experimental results and the viscoplastic model. The profile shapes show promising comparisons with the viscoplastic model for the shallowest depth $h_0 = 1\text{cm}$, however highlight the need to measure more accurately the rheology of the substrate. The dropping experiments also nicely demonstrate the relationship between initial speed $\dot{\delta}_0$ and the final depth of indentation δ_f .

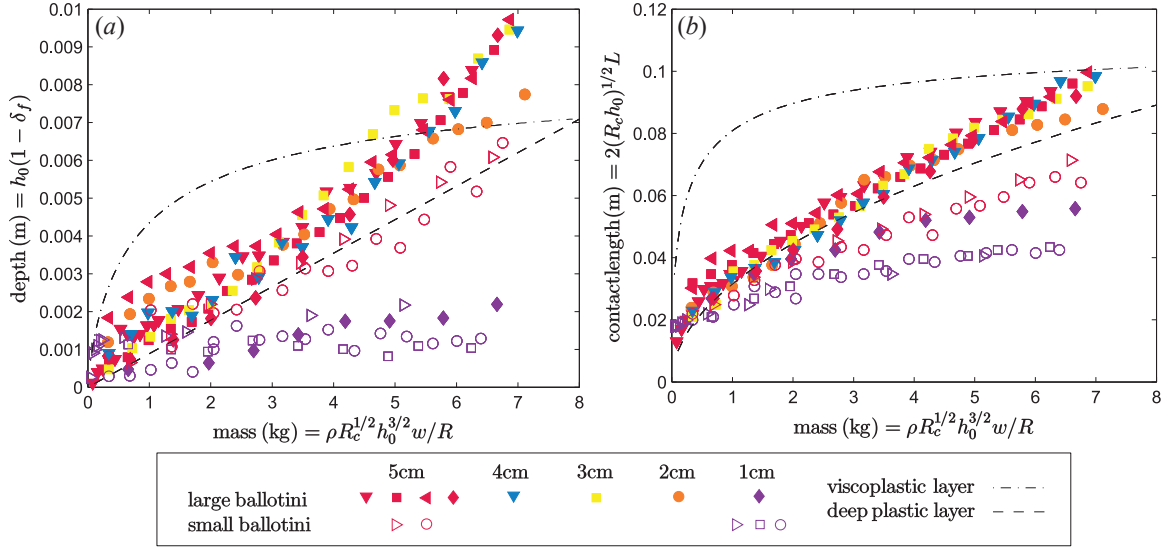


Figure 10: Loading experiments for a cylinder indenting a layer of ballotini of height $h_0 = 1 - 5$ cm. (a) Depth and (b) contact length with mass for small 0.2mm diameter (empty points) and large 1mm diameter (filled points) ballotini. Theoretical curves for the deep plastic layer (black dashed lines) and viscoplastic layer (black dot-dashed lines) are plotted for parameters $\phi = 24.9$, $\rho = 1550 \text{ kgm}^{-3}$, $N_\gamma = 6.5$, $h_0 = 0.01 \text{ m}$, $R_c = 0.076 \text{ m}$ and $w = 0.2 \text{ m}$.

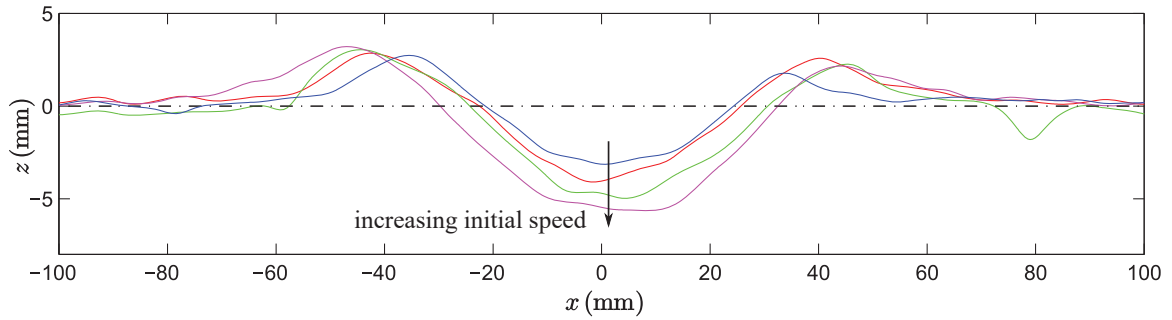


Figure 11: Profiles of dropping experiments for a substrate of 1mm ballotini with depth $h_0 = 5$ cm. Coloured lines indicate different initial heights of the cylinder above the surface, and hence different initial speeds δ_0 .

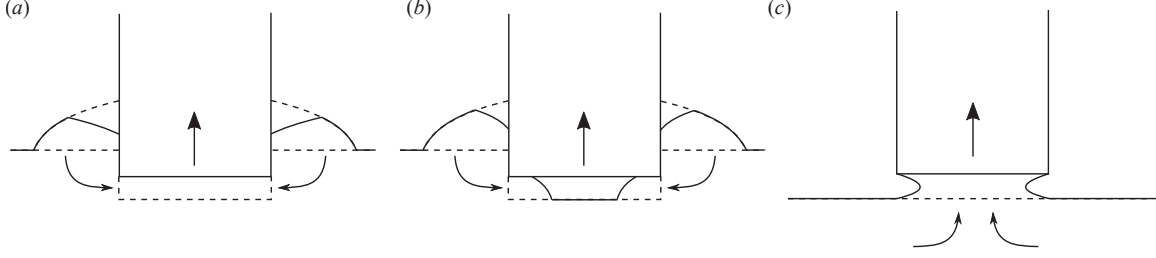


Figure 12: Schematic of methods of lift off: (a) reverse squeeze flow, (b) avalanching, and (c) adhesion.

4 Theoretical Model: Lift Off

We now consider the second stage of our theoretical model: lift off, where the indenter lifts off the deformed substrate at a given speed. This stage describes the final indentation left after the indenter has been removed. We consider three methods of lift off: (a) reverse squeeze flow, (b) avalanching and (c) adhesion, see figure 12. We will primarily consider the lift off of a flat-based indenter; however, the methods used could easily be applied to more complicated geometries such as a parabola as discussed previously.

4.1 Reverse squeeze flow

The first method of lift off considers when no air can get underneath the indenter. Instead, as the indenter is lifted above its final resting depth δ_f a reverse squeeze flow is generated in which material from the outside free-surface flow is pulled underneath to fill the gap. We assume final lift off can occur when the free surface outside meets the corner of the indenter i.e. pressure is atmospheric. Figure 13(a) shows the final stage of lift off when the indenter can detach from the substrate. At this point the depth of the indentation has raised from the δ_f to δ_l with the excavated mound of material outside meeting the flat base at $x = 1$.

4.1.1 Purely cohesive, $\tau_Y = \text{constant}$

From section 2.3.5, the free-surface before lift off is given by

$$h = \left(h_L^2 + \frac{2B}{R}(1-x) \right)^{1/2}. \quad (69)$$

Provided the speed of lift off is sufficiently slow that the free-surface flow remains in the plastic limit, the free-surface profile steps through a series of static shapes with the final profile given by

$$h = \begin{cases} \left(h_L^2 + \frac{2B}{R}(1-x) \right)^{1/2} & 1 < x < L_f, \\ \left(\delta_L^2 + \frac{2B}{R}(x-1) \right)^{1/2} & L_f < x < L_0, \end{cases} \quad (70)$$

see figure 13(a). To find δ_L mass conservation is used, which in the plastic limit is an equal areas construction given the quasistatic free-surface profiles. Hence by global conservation

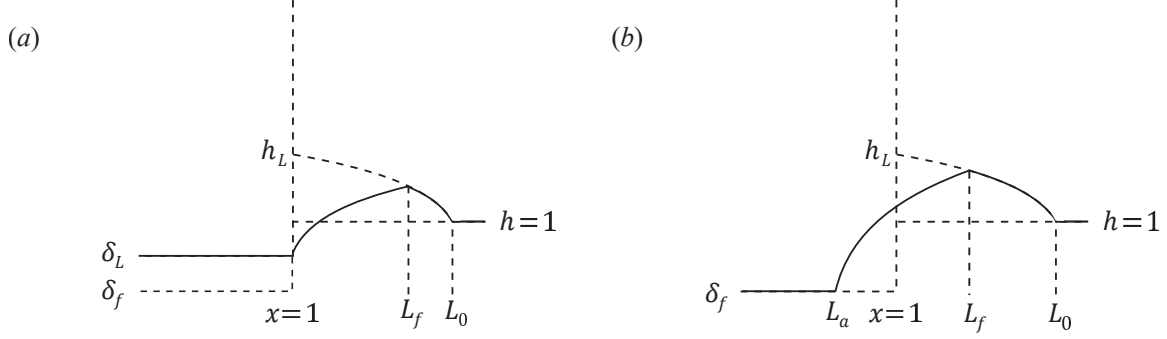


Figure 13: Schematic of the parameters for (a) the reverse squeeze flow, and (b) the avalanching method.

of mass, the free-surface profile can be integrated to give

$$\delta_L - \delta_f = \frac{R}{3B} \left(h_L^3 + \delta_L^3 - 2 \left(\frac{1}{2} (h_L^2 + \delta_L^2) \right)^{3/2} \right), \quad (71)$$

using $h_L^2 + \frac{2B}{R}(1 - L_f) = \delta_L^2 + \frac{2B}{R}(L_f - 1)$. Calculating δ_f and h_L from section 2, the depth δ_L can be determined as a function of B and R . Figure 14(a) plots the final profile for two sets of parameters, $B = 2$, $R = 1$ (red lines) and $B = 1$, $R = 2$ (blue lines).

4.1.2 Mohr-Coulomb, $\tau_Y = p \tan \phi$

For the Mohr-Coulomb case, the free-surface profile before lift off is given by

$$h = h_L + \Phi(1 - x), \quad (72)$$

see section 2.5.4. As in the pure cohesion case, for a sufficiently slow lift off speed the free-surface flow remains in the plastic limit and hence can be written as (figure 13(a)).

$$h = \begin{cases} h_L + \Phi(1 - x) & 1 < x < L_f, \\ \delta_L + \Phi(x - 1) & L_f < x < L_0, \end{cases} \quad (73)$$

Integrating the free-surface profile after lift off gives an equation relating δ_L , δ_f and h_L ,

$$\delta_L - \delta_f = \frac{(h_L - \delta_L)^2}{4\Phi}. \quad (74)$$

As in the pure cohesion case, together with the depth δ_f and height h_L from section 2, the depth δ_L can be determined as a function of Φ and R .

4.2 Avalanching

The second method of lift off considers when air can get underneath the indenter. When the indenter is lifted off the substrate, the gap between the indenter and the final depth δ_f is filled with air in the interior with ‘avalanching’ regions near the edge where there is a squeeze flow and free surface flow, see figure 12(b). When the indenter is removed, the base of the indentation remains at δ_f with the mound of material outside now meeting the base at $x = L_a < 1$ (figure 13(b)).

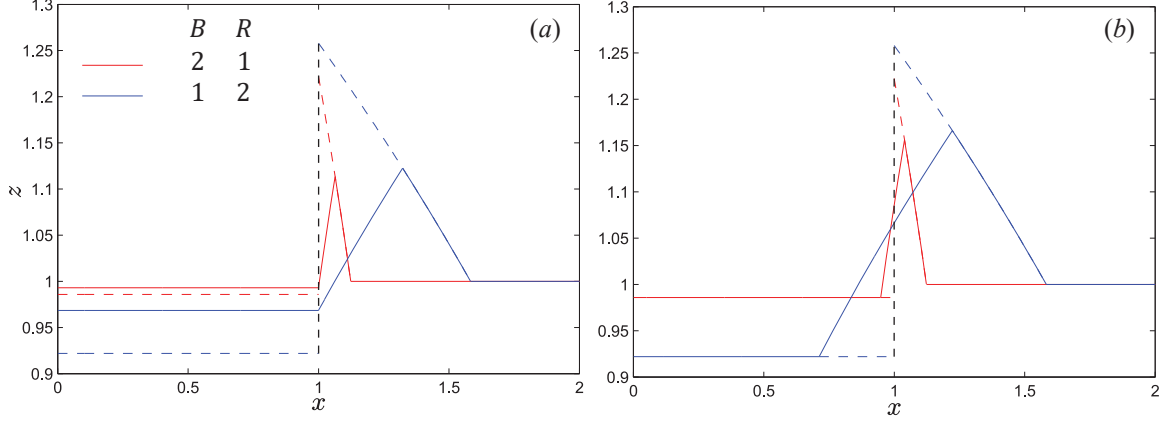


Figure 14: Plot of final indentation for the pure cohesion model after lift off for (a) squeeze flow method, and (b) avalanching method for parameters $B = 2, R = 1$ (red lines) and $B = 1, R = 2$ (blue lines). The profiles before and after lift off are given by the dashed and solid lines respectively.

4.2.1 Purely cohesive, $\tau_Y = \text{constant}$

In the plastic limit, the profile of the free-surface can be written as

$$h = \begin{cases} \left(\delta_f^2 + \frac{2B}{R}(x - L_a) \right)^{1/2} & L_a < x < L_f, \\ \left(h_L^2 + \frac{2B}{R}(1 - x) \right)^{1/2} & L_f < x < L_0. \end{cases} \quad (75)$$

Using global mass conservation to match the areas of slumped material then gives

$$\frac{R}{3B} (h_L^3 + \delta_f^3) + (1 - L_a) = \frac{2R}{3B} \left[\frac{h_L^2 + \delta_f^2}{2} + \frac{B}{R}(1 - L_a) \right]^{3/2}. \quad (76)$$

And hence, using δ_f and h_L calculated in section 2, L_a can be found as a function of B and R . Figure 14(b) plots the final profile for the two sets of parameters $B = 2, R = 1$ (red lines) and $B = 1, R = 2$ (blue lines).

4.2.2 Mohr-Coulomb, $\tau_Y = p \tan \phi$

The profile of the free-surface can be written as

$$h = \begin{cases} h_L + \Phi(1 - x) & L_a < x < L_f \\ \delta_f + \Phi(x - L_a) & L_f < x < L_0 \end{cases} \quad (77)$$

Using global mass conservation to match the areas of slumped material then gives

$$(h_L - \delta_f)(h_L - h_f) - \frac{1}{2}(h_L - h_f)^2 - \frac{1}{2}(h_f - \delta_f)^2 = 0, \quad (78)$$

where $h_f = h_L + \Phi(1 - L_f) = \delta_f + \Phi(L_f - L_a)$. Together with δ_f and h_L calculated in section 2, L_a can be found as a function of parameters Φ and R .

4.3 Adhesion

In both the reverse squeeze flow and the avalanching method, we have assumed that lift off happens completely when the pressure at the edge of the indenter $x = 1$ is atmospheric i.e. when the free-surface reaches the corner. A non-cohesive material has no strength in tension, therefore you would expect this to be the case. For a cohesive material however, there would be some adhesion to the indenter. When thinking about track making, this adhesion must be able to be characterised in the form of a pressure or stress condition on the base allowing lift off at some point. In the experiments described in the next section we have only considered a non-cohesive material, therefore adhesion is not applicable.

4.4 Experiments

To investigate the lift off stage experimentally we used the setup as described in section 3 with a layer of 1mm diameter ballotini of depth $h_0 = 5\text{cm}$. As the ballotini is dry, we would anticipate that air can get in between the particles and underneath the indenter during lift off. And hence, we expect the method of lift off to be as described in section 4.2 with the bottom of the indentation remaining the same while avalanching occurs on the sides.

Figure 15 shows two lift off experiments with different initial depths for a cylindrical indenter. Figure 15(a,b) plot the detected profiles before (blue solid line) and after (red solid line) lift off together with the free-surface profile for a non-cohesive material with angle of friction $\phi = 24.9 \pm 0.7$ (black dot-dashed line), see equation (49). The corresponding photographs, figure 15(c,d) are taken after lift off to demonstrate the final profile. In the first experiment, figure 15(a), the indentation is sufficiently shallow that the sides of the indentation remain roughly at or below the angle of friction. As a result, almost no avalanching occurs as seen by the negligible difference between the before and after profiles. When the indentation depth is increased, the walls become steeper than the angle of friction at the contact points, see figure 15(b). In this case, when lift off occurs, the ballotini avalanches down into the interior of the indentation with the bottom of the indentation remaining fixed. Figure 15(b) suggests that the final profile then sits at an angle less than the angle of friction. This may be due to any added inertia caused by the process of lift off.

In this section we have considered a simple theoretical model to describe the process of lift off for a flat-based indenter on either a purely cohesive or Mohr-Coulomb substrate. We have looked at three different methods for lift off: (a) reverse squeeze flow, (b) avalanching and (c) adhesion. Our preliminary experiments with dry ballotini demonstrate the method of avalanching when air can get underneath the indenter. To explore the process of lift off further we need to consider the problem of adhesion and the point at which completed detachment from the substrate can occur.

5 Conclusion

The aim of this work was to understand the indentation of deformable plastic layers theoretically and experimentally. Our theoretical model using viscoplastic lubrication theory describes the indentation of a shallow plastic layer. We have shown that the plastic limit reduces to a force balance and equal areas construction given the quasistatic free-surface

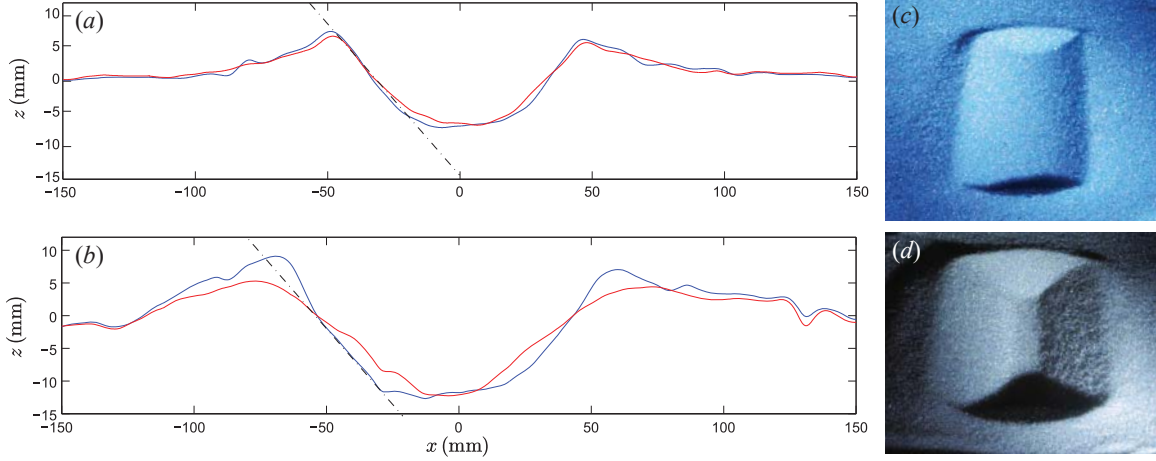


Figure 15: Lift off experiments with a layer of 1mm ballotini of depth $h_0 = 5\text{cm}$. (a,b) Depth profiles for increasing depths of indentation for before (blue solid line) and after (red solid line) lift off. Black dot-dashed line indicates theoretical angle of friction $\phi = 24.9 \pm 0.7$. (c,d) Photographs of final profiles for experiments shown in (a,b), respectively.

profiles. The simple experimental setup used has produced promising preliminary results for the indentation of a pure cohesive (joint compound) and non-cohesive (ballotini) substrate with some qualitative comparisons with our theoretical model.

To extend this work in future, we plan on conducting further experiments to investigate the indentation of deformable plastic layers. In terms of a pure cohesive material we would like to better characterise the yield stress of the substrate and confirm that a Bingham rheology is an appropriate approximation opposed to a more complicated Herschel-Bulkley model. In addition, we would like to characterise the discrepancy between ballotini sizes to check initial conditions resetting the surface are not playing a role. In terms of experimental setup, we would like to improve the simple system to reduce the compliance of the indenter, for example by clamping the sizes of half cylinder, and extending to axisymmetric geometries such a hemisphere. Finally, when discussing the problem of lift off, we touched on the case of adhesion. This needs to be explored further both theoretically and experimentally as the process of lift off ultimately determines the final indentation left behind.

6 Acknowledgments

I would like to thank Neil Balmforth and Ian Hewitt for their thorough supervision throughout the summer and tireless enthusiasm to find some ‘good mud’!

References

- [1] J. R. L. ALLEN, *Subfossil mammalian tracks (Flandrian) in the Severn Estuary, S. W. Britain: mechanics of formation, preservation and distribution*, *Phi. Trans. R. Soc. Lond.*, 352 (1997), pp. 481–518.
- [2] K. T. BATES, R. SAVAGE, T. C. PATAKY, S. A. MORSE, E. WEBSTER, P. L. FALKINGHAM, L. REN, Z. QIAN, D. COLLINS, M. R. BENNETT, J. MCCLYMONT, R. H. CROMPTON, M. SA, E. WEBSTER, F. PL, Z. QIAN, D. COLLINS, AND J. MCCLYMONT, *Does footprint depth correlate with foot motion and pressure?*, *J. R. Soc. Interface*, (2013).
- [3] M. D. BOLTON AND C. K. LAU, *Vertical bearing capacity factors for circular and strip footings on Mohr-Coulomb soil*, *Can. Geotech. J.*, 30 (1993), pp. 1024–1033.
- [4] I. F. COLLINS, *A Simplified Analysis of the Rolling of a Cylinder on a Rigid/Perfectly Plastic Half-Space*, *Int. J. Mech. Sci.*, 14 (1972), pp. 1–14.
- [5] N. DUBASH, N. BALMFORTH, A. SLIM, AND S. COCHARD, *What is the final shape of a viscoplastic slump?*, *J. Nonnewton. Fluid Mech.*, 158 (2009), pp. 91–100.
- [6] G. EASON AND R. T. SHIELD, *The plastic indentation of a semi-infinite solid by a perfectly rough circular punch*, *Z. Angew. Math. Phys.*, 11 (1960), pp. 33–43.
- [7] D. D. GILLETTE AND M. G. LOCKLEY, *Dinosaur tracks and traces*, Cambridge University Press, 1991.
- [8] I. J. HEWITT AND N. J. BALMFORTH, *Viscoplastic lubrication theory with application to bearings and the washboard instability of a planing plate*, *J. Nonnewton. Fluid Mech.*, (2012), pp. 1–17.
- [9] R. HILL, *The mathematical theory of plasticity*, vol. 11, Oxford university press, 1950.
- [10] K. LIU AND C. MEI, *Approximate equations for the slow spreading of a thin sheet of bingham plastic fluid*, *Phys. Fluids A*, 2 (1990), pp. 30–36.
- [11] E. A. MARSHALL, *Rolling contact with Plastic Deformation*, *J. Mech. Phys. Solids.*, 16 (1968), pp. 243–254.
- [12] J. MILÀN, *Variations in the Morphology of Emu (*Dromaius Novaehollandiae*) Tracks Reflecting Differences in Walking Pattern and Substrate Consistency: Ichnotaxonomic Implications*, *Palaeontology*, 49 (2006), pp. 405–420.
- [13] J. NYE, *Plasticity solution for a glacier snout*, *J. Glaciol.*, 6 (1967), pp. 695–715.
- [14] L. PRANDTL, *Über die harte plastischer körper, nachrichten von der königlichen gesellschaft der wissenschaften zu gottingen*, *Math. Phys. KI*, 12 (1920), pp. 74–85.
- [15] J. SALENÇON, *Bearing capacity of a footing on an angle of shearing resistance = 0 soil with linearly varying shear strength*, *Geotechnique*, 24 (1974).

- [16] R. T. SHIELD. *On the plastic flow of metals under conditions of axial symmetry*. Proc. Royal Soc. A, 233 (1955), pp. 267-287.
- [17] A. J. M. SPENCER, *Perturbation methods in plasticity - I plane strain of non-homogenous plastic solids*, J. Mech. Phys. Solids, 9 (1961), pp. 279-288.
- [18] ———, *Perturbation Methods in Plasticity - II Plane Strain of Slightly Irregular Bodies*, Mech. Phys. Solids, 10 (1962), pp. 17-26.
- [19] K. TERZAGHI, *Theoretical Soil Mechanics*, John Wiley & Sons, Inc., 1943.